BMC Medicine

RESEARCH

Open Access

MTHFD2 promotes osteoclastogenesis and bone loss in rheumatoid arthritis by enhancing CKMT1-mediated oxidative phosphorylation

Yujing Li[1], Minglong Cai[1], Yi Qin[1,2], Xiaojuan Dai[1], Liyuan Liang[3], Zhenyu Li[1], Xi Wen[1], Huizhi Jin[1], Chao Yang[4*†] and Zhu Chen[1*†]

Abstract

Background Rheumatoid arthritis (RA) is a chronic autoimmune disease characterized by disrupted bone homeostasis. This study investigated the effect and underlying mechanisms of one-carbon metabolism enzyme methylenetetrahydrofolate dehydrogenase 2 (MTHFD2) on osteoclast differentiation and bone loss in RA.

Methods The expression of MTHFD2 was examined in CD14 + monocytes and murine bone marrow-derived macrophages (BMMs). RNA-sequencing was performed to evaluate the regulatory mechanisms of MTHFD2 on osteoclastogenesis. Extracellular flux assay, JC-1 staining, and transmission electron microscopy were used to detect mitochondrial function and energy metabolism changes during osteoclast formation. Collagen-induced arthritis (CIA) mice were used to evaluate the therapeutic effect of MTHFD2 knockdown on bone loss. Bone volume and osteoclast counts were quantified by μCT and histomorphometry.

Results Elevated MTHFD2 was observed in RA patients and CIA mice with a positive correlation to bone resorption parameters. During osteoclast formation, MTHFD2 was significantly upregulated in both human CD14 + monocytes and murine BMMs. The application of MTHFD2 inhibitor and MTHFD2 knockdown suppressed osteoclastogenesis, while MTHFD2 overexpression promoted osteoclast differentiation in vitro. RNA-sequencing revealed that MTHFD2 inhibition blocked oxidative phosphorylation (OXPHOS) in osteoclasts, leading to decreased adenosine triphosphate (ATP) production and mitochondrial membrane potential without affecting mitochondrial biogenesis. Mechanistically, inhibition of MTHFD2 downregulated the expression of mitochondrial creatine kinase 1 (CKMT1), which in turn affected phosphocreatine energy shuttle and OXPHOS during osteoclastogenesis. Further, a therapeutic strategy to knock down MTHFD2 in knee joint in vivo ameliorated bone loss in CIA mice.

Conclusions Our findings demonstrate that MTHFD2 is upregulated in RA with relation to joint destruction. MTHFD2 promotes osteoclast differentiation and arthritic bone erosion by enhancing mitochondrial energy metabolism

†Chao Yang and Zhu Chen contributed equally to this work.

*Correspondence:
Chao Yang
ychmax@xjtufh.edu.cn
Zhu Chen
doczchen@ustc.edu.cn
Full list of author information is available at the end of the article

through CKMT1. Thus, targeting MTHFD2 may provide a potential new therapeutic strategy for tackling osteoclastogenesis and bone loss in RA.

Keywords Rheumatoid arthritis, Osteoclast differentiation, Methylenetetrahydrofolate dehydrogenase 2, Oxidative phosphorylation

Background

Rheumatoid arthritis (RA) is a chronic, systemic autoimmune disease characterized by symmetric synovial inflammation and imbalanced bone homeostasis [1]. Over 45% RA patients are reported to exhibit bone erosion at an early stage or even before the appearance of the first clinical symptoms [2]. Bone destruction progresses in time and contributes to joint damage and impaired functional capacity in patients with RA, constituting a critical contributor to disability [3, 4]. Furthermore, bone erosions are indicative of a more severe clinical course, establishing them as a critical outcome marker for RA patients [5].

Bone homeostasis depends on the equilibrium of osteoblast-mediated bone formation and osteoclast-triggered bone resorption [6]. In RA patients, coordinated bone metabolism is disrupted, as osteoclasts increase in number and are functionally overactive, resulting in local and systemic bone loss [2]. However, the mechanisms driving uncontrolled osteoclastogenesis and subsequent bone destruction in RA remain incompletely understood. In recent years, inhibition of osteoclast formation by biologic disease-modifying antirheumatic drugs (bDMARDs) such as interleukin-6 blocking agents and anti-tumor necrosis factor-α antibodies has shown promising effects [7]. Denosumab, an anti-receptor activator of nuclear factor-κB ligand (RANKL) antibody, has demonstrated efficacy in inhibiting the progression of osteoclast-mediated bone erosion and enhancing bone mineral density (BMD) in RA patients [8–10]. However, a proportion of patients are refractory to multiple bDMARDs [11]. Additionally, intolerable side effects and the rebound effect following the denosumab discontinuation restrict the application of these treatments [12, 13]. Therefore, comprehensive understanding of the molecular mechanisms underlying osteoclast differentiation and resorptive activity is pivotal to design novel therapeutic targets for RA.

Proper mitochondrial metabolism is essential for osteoclastogenesis and bone loss [14, 15]. Methylenetetrahydrofolate dehydrogenase 2 (MTHFD2) is an essential enzyme of mitochondrial one-carbon (1C) metabolism, catalyzing the interconversion of 5,10-methylene-THF to 10-formyl-THF and generating formate for de novo purine synthesis [16]. 1C metabolism comprises a series of interconnected metabolic pathways, including folate cycle, methionine cycle and transsulfuration pathway [17]. Evidence suggests a correlation between 1C metabolism and RA [18–21]. Previous reports showed that genetic variations of 5,10-methylenetetrahydrofolate reductase, a critical enzyme for intracellular folate homeostasis, linked to increased susceptibility to RA [18, 19]. In addition, low doses of the antifolate drug methotrexate (MTX), which inhibits dihydrofolate reductase (DHFR) in 1C metabolism, has long been used as an anchor DMARD in the management of RA [20, 21]. However, adverse effects involving mucosal, gastrointestinal, hepatic or hematologic toxicities are commonly observed in patients treated with MTX, partly attributed to the broad expression of DHFR in all dividing cells [22, 23]. In contrast to DHFR, MTHFD2 is highly expressed in cancer cells and immune cells while is ordinarily low or absent in normal adult tissues [24]. Given the narrower range of cells that express this enzyme, MTHFD2 is an ideal target for treating cancer and autoimmune diseases. However, the roles of MTHFD2 in osteoclastogenesis and bone resorption remain unknown. We, therefore, tested the hypothesis that MTHFD2 orchestrates osteoclast formation and inflammatory bone erosion in RA patients.

Methods

Human sample collection

Peripheral blood and synovial specimens were donated from healthy donors (HDs), osteoarthritis (OA) and RA patients at the First Affiliated Hospital of USTC (University of Science and Technology of China). The inclusion criteria were RA patients that aged 18 years older and fulfilled the 2010 defined RA classification criteria of the American College of Rheumatology (ACR)/ European League Against Rheumatism (EULAR) [25]. Exclusion criteria included a history of renal or hepatic diseases, severe infection, malignant tumors, and other rheumatic-inflammatory diseases. All patients provided written informed consent to participate in the present study. All protocols were approved by the Research Ethics Committees of the First Affiliated Hospital of USTC. The procedures complied with the principles of the Declaration of Helsinki.

Isolation of peripheral blood CD14 + monocytes

Peripheral blood mononuclear cells (PBMCs) were isolated from whole blood collected from the HDs and

RAs by Ficoll-Hypaque density-gradient centrifugation (Sigma-Aldrich). CD14 + monocytes were isolated using CD14 + magnetic bead separation according to the manufacturer's instructions (Miltenyi Biotech). CD14 + monocytes were stained with fluorescein isothiocyanate-conjugated anti-CD14 antibody (BD Biosciences) for flow cytometric analysis.

Enzyme-linked immunosorbent assay (ELISA) assay

RA serum was collected and the serum levels of the bone resorption marker collagen C-terminal telopeptides of type I collagen (CTX-1) and active isoform 5b of tartrate-resistant acid phosphatase (TRAP) were measured using ELISA kits (AC-02F1 and SB-TR201A, Immunodiagnostics Systems, Maryland, USA) according to the manufacturer's instructions.

Bone marrow macrophage (BMM) isolation and osteoclast differentiation

BMMs were isolated from 6-week-old wildtype (WT) male C57BL/6 J mice by flushing the femur and tibia. After removing red blood cells, BMMs were incubated in complete α minimum essential medium (α-MEM) (Gibco) at 37 °C overnight. After that, nonadherent cells were collected and further cultured in complete α-MEM with M-CSF (30 ng/mL) and RANKL (50 ng/mL) (PeproTech) supplemented or not with 10 μM MTHFD2i (MedChemExpress) in mice osteoclast medium. New media, cytokines and inhibitor were replenished every 2 days. TRAP staining was performed on day 5 when osteoclasts were fully differentiated using the TRAP kit (Servicebio, Wuhan, China) following the manufacturer's instructions. TRAP-positive cells with three or more nuclei were considered osteoclasts and were counted. For human osteoclast differentiation, CD14 + monocytes were cultured in complete α-MEM with M-CSF (30 ng/mL) and RANKL (50 ng/mL) (PeproTech) supplemented or not with 7.5 μM MTHFD2i in human osteoclast medium and mature osteoclasts were characterized by TRAP staining on day 10. For bone resorption assay, 1×10^5 BMMs were seeded onto bovine cortical bone slices at the bottom of 96-well culture plates. Resorption pits of osteoclasts on the slices were shown by scanning electron microscopy.

Cell viability test

1×10^5 cells were cultured in 96-well plates with 30 ng/mL M-CSF and 50 ng/mL RANKL with or without different concentrations of MTHFD2i. Cell viability test was performed on day 6 and day 9 for CD14 + monocyte-derived osteoclast precursors (OCPs) and on day 3 for BMM-derived OCPs. After indicated time, non-adherent cells in a 96-well plate were washed twice using PBS. Then cells were stained with 50 μL 0.5% crystal violet staining solution for 20 min at room temperature with gentle shake. The plate was then washed by PBS for four times and airdried for at least 1 h. Then, 200 μL methanol was added to each well. The plate was incubated for 20 min at room and then measured at 570 nm with a plate reader.

RNA extraction and quantitative real-time polymerase chain reaction (qRT-PCR)

Total RNA was extracted using the HiPure Total RNA Mini Kit (Magen, China) according to the manufacturer's instructions. The concentration and purity of the mRNA were assessed by a Nanodrop spectrophotometer. Then mRNA was reverse transcribed to cDNA with the FastKing gDNA Dispelling RT Supermix (Tiangen, China). qRT-PCR was performed using the QuantiNova SYBR Green PCR Kit (QIAGEN, Germany) on the QuantStudio Q5 PCR system. Samples were analyzed in duplicate and normalized to the level of β-actin mRNA for murine and human samples. Relative gene expression was calculated by the $2^{-\Delta\Delta Ct}$ method. Human and murine qPCR primer sequences are listed in Additional file 1: Table S1.

Western blot

For western blot, cells were lysed with radioimmunoprecipitation assay buffer supplied with phosphatase inhibitor cocktail and protease inhibitor cocktail (Epizyme, Shanghai, China). The protein extracts were then separated by SDS-PAGE electrophoresis and transferred to a polyvinylidenedifluoride membrane (Millipore, Massachusetts, USA). Antigen detection was performed using antibodies directed against MTHFD2 (Proteintech, 12270–1-AP), c-Src (Proteintech, 11097–1-AP), CTSK (Cell Signaling, #57,056), β3 integrin (Epizyme, R013849), MMP9 (Abcam, ab228402), OXPHOS (Abcam, ab110413), CKMT1 (Proteintech, 15346-1-AP), VDAC (Epizyme, R012378), Tomm20 (Epizyme, R013740), PGC1β (Proteintech, 22378–1-AP), phospho-AMPK alpha 1 (Ser496) (Epizyme, R011713), AMPK alpha 1 (Cell Signaling, #5832), phospho-mTOR (Cell Signaling, #5536), mTOR (Cell Signaling, #2983) or β-actin (Proteintech, HRP-60008) overnight at 4 °C, followed by probing with fluorescence-labeled secondary antibodies. To observe the results, chemiluminescence detection system (Bio-Rad) was used.

Immunofluorescence staining

For F-actin staining, osteoclasts were fixed with 4% paraformaldehyde, permeabilized with 0.1% Triton X-100 and then incubated with Alexa Fluor 488- or Alexa Fluor 633-conjugated phalloidin (Solarbio) for 30 min. For Mitotracker Green staining, live cells were incubated with 100 nM Mitotracker Green (Beyotime) in

pre-warmed α-MEM for 30 min at 37 °C in the dark. For JC-1 staining, OCPs after 48 h stimulation with RANKL and DMSO or MTHFD2i were washed and then stained with JC-1 Assay Kit (Beyotime) for 20 min at 37 °C in the dark. For mitochondrial superoxide staining, OCPs after 48 h simulation with RANKL and DMSO or MTHFD2i were washed with warm α-MEM and stained with MitoSOX™ Red Mitochondrial Superoxide Indicator (Invitrogen) according to the manufacturer's instructions. For flow cytometry assay of MitoSOX staining, cells were detached and centrifuged at 400 *g* for 5 min. Then, cells were subjected to flow cytometry analysis on Cytoflex LX (Beckman-Coulter). Fluorescence images were acquired with a Zeiss laser confocal microscope and analyzed with ImageJ software.

Lentiviral gene transduction and short hairpin RNA (shRNA) adenoviral knockdown

Short-hairpin RNA targeting *MTHFD2* and scrambled shRNA (GenePharma) were bought from the Shanghai Hanbio Co., Ltd. MTHFD2-overexpressing lentivirus was bought from the Shanghai GeneChem Co., Ltd. The target sequences for mouse MTHFD2 knockdown were CACACGATCCTTGCAGACATTGTAA. Cells were washed and cultured in low-serum media (5% FBS) with lentiviral (MOI = 80) or adenoviral particles (MOI = 500) in the presence of 4 μg/ml polybrene (Hanbio, Shanghai, china) for 16 h. Efficiency of overexpression and shRNA knockdown was confirmed by Western blot 48 to 72 h later.

Transcriptome analysis

BMMs were cultured in the presence of M-CSF and RANKL with or without MTHFD2i for 2 days. Afterward, cells were collected and total RNA was isolated using TRIzol reagent. RNA-seq analyses were entrusted to a professional biological company (Oebiotech, Shanghai, China). Genes with a fold change of 2 were considered as differentially expressed genes (DEGs) and analyzed using the DAVID Bioinformatics Resources 6.8. Among the DEGs, we performed Gene Ontology (GO) analysis and Kyoto Encyclopedia of Genes and Genomes (KEGG) enrichment analysis by Rstudio and Gene Set Enrichment Analysis (GSEA) software.

Mitochondrial oxygen consumption rate (OCR) measurement

The mitochondrial respiratory activity was assessed by measuring OCR on Seahorse XFe96 Analyzer (Agilent, USA). Seahorse XF Cell Mito Stress test kit (Agilent, USA) was used according to the manufacturer's instructions. Briefly, an equal number of OCPs were seeded on XFe96 cell culture microplates (Agilent) at a seeding density of 8×10^4 cells per well after stimulation with M-CSF and RANKL for 2 days, with or without MTHFD2i treatment. Before the assay, culture media was changed to XF DMEM (pH 7.4) supplemented with 1 mM sodium pyruvate, 2 mM glutamine, and 10 mM glucose. After 30-min pre-equilibration in a 37 °C non-CO_2 incubator, OCR was measured at 37 °C by using following drugs: 1 μM oligomycin, 2 μM Trifluoromethoxy carbonyl cyanide phenylhydrazone, and 1 μM rotenone/antimycin A. Mitochondrial respiration parameters were further calculated by the Wave software as described previously [26].

Adenosine triphosphate (ATP) quantification assay

Intracellular ATP level was quantified using an ATP Determination Kit (Beyotime, China) according to the manufacturer's instructions. Briefly, cultured cells or standard solution together with reaction mixture were added to the 96-well cell culture plate. After 10-min incubation, the plate was read using a luminescence detector. Intracellular ATP concentrations were then calculated using the standard curve.

Transmission electron microscopy (TEM)

1×10^6 OCPs at day 3 after culture with 50 ng/mL RANKL and DMSO or MTHFD2i were washed with PBS and fixed with 2.5% glutaraldehyde in 0.1 M phosphate buffer at 4 °C for 48 h. Then the cells were post-fixed, stained and imaged as described before [15].

Creatine kinase activity assay

OCPs were lysed in the lysis buffer provided in the Creatine Kinase Activity Assay Kit (Solarbio) and cellular creatine kinase activity was examined according to the manufacturer's instructions.

Collagen-induced arthritis (CIA) model

All animal experiments were approved by the Animal Ethics Committee of the First Affiliated Hospital of USTC. CIA was induced in 8-week-old male DBA/1 J mice by subcutaneous injection at the base of the tail with 100 μL 2 mg/mL chicken type II collagen (Chondrex) in complete or incomplete Freund adjuvant (Chondrex) at day 0 and day 21, respectively. The clinical severity of CIA was assessed every 3 days starting on day 21. Each paw was scored using a 4-point scale: 0, normal; 1, minimal swelling or redness; 2, obvious redness and swelling involving the entire forepaw; 3, severe redness and swelling with limited movement; 4, joint deformity or ankylosis or both [27].

Adeno-associated virus (aav) treatment

In vivo knockdown of MTHFD2 was achieved using aav9 vectors. Murine MTHFD2-knockdown aav9 (aav-MTHFD2) and the corresponding control aav9 (aav-ctrl) were manufactured by Hanbio (Shanghai, China). CIA mice were randomly divided into different groups and then received knee joint injection of 5 μL aav (titer = 1×10^{12}) viral particles of aav-MTHFD2 or aav-ctrl at day 7 post first immunization. Before injection, mice were anesthetized with isoflurane.

Micro-computed tomography

μCT scanning was performed as previously described [28]. Briefly, hind limbs of CIA mice were fixed in 4% paraformaldehyde and scanned with Micro-CT (Pingsheng Healthcare Shanghai Inc., Shanghai, China) with the following scan parameters: 80 kV, 80 μA and 13 μm per pixel resolution. Images were 3D reconstructed and visualized by NRecon and Avatar software, respectively. For analyzing bone volume, the region of interest was computed for the following bone morphometric variables: bone volume/total volume (BV/TV), trabecular bone number (Tb.N), trabecular bone thickness (Tb.Th), trabecular bone separation (Tb.Sp), and BMD.

Bone histomorphometric analysis

CIA mice were sacrificed on day 42. Tibia were fixed overnight in 4% formalin followed by 3-week defalcation in EDTA until bones were pliable. Then osteoclasts and osteoblasts were identified by TRAP staining, osteocalcin (OCN) immunohistochemistry (IHC), and Toluidine Blue staining as previously described [29]. To quantify for histomorphometric parameters, images for each bone slice were captured blindly through light microscopy (Olympus, Japan) and three fields of view in the proximal tibia were randomly selected. In each view, trabeculae were outlined and osteoclasts or osteoblasts were traced. Then, the quantitative parameters, including osteoclast surface/bone surface (Oc.S/BS), osteoclast number/bone perimeter (N.Oc./B.Pm.) and osteoblast surface/bone surface (Ob. S/BS) were automatically analyzed with OsteoMeasure image analysis system (OsteoMetrics, USA).

Statistical analysis

Quantitative data are presented as the mean ± standard deviation. Statistical analysis between two groups was conducted using two-tailed Student's *t* test. One-way analysis of variance (ANOVA) was used to compare multiple groups, followed by Tukey's test. The correlation of MTHFD2 gene expression in human CD14 + monocytes with serum CTX-1 and TRAP5b levels was assessed by Spearman's correlation test. Pearson's correlation test was used to describe correlations between mice MTHFD2 gene expression and osteoclast-specific gene expression. Analysis of all statistical data was carried out using GraphPad Prism (version 9.0). In all experiments, $p < 0.05$ was regarded as statistically significant. For all experiments, $^{*}p < 0.05$, $^{**}p < 0.01$, $^{***}p < 0.001$, and $^{****}p < 0.0001$. All representative experiments shown were repeated three or more times independently.

Results

MTHFD2 is highly expressed in OCPs and is positively correlated with osteoclast differentiation

To assess MTHFD2 expression in OCPs under pathological conditions, PBMCs and circulating CD14 + monocytes were isolated from RA patients and sex-matched HDs. Flow cytometry confirmed a purification rate of > 90% for CD14 + PBMCs (Additional file 1: Fig. S1). As depicted in Fig. 1A, the mRNA level of MTHFD2 was significantly elevated in PBMCs and CD14 + monocytes of RA patients compared to HDs. BMMs were obtained from WT and CIA mice. MTHFD2 was also highly expressed in BMMs of CIA mice than that of WT mice (Fig. 1B). To investigate the relationship between MTHFD2 expression in circulating OCPs and bone erosion in RA, 22 patients with RA were included for statistical analysis. We observed that there was a positive correlation between MTHFD2 mRNA level in peripheral blood CD14 + monocytes and CTX-1 ($r = 0.5848$, $p = 0.0043$) and TRAP5b ($r = 0.4799$, $p = 0.0238$), both

(See figure on next page.)

Fig. 1 Expression of MTHFD2 in human and murine OCPs and MTHFD2 level during osteoclastogenesis. **A** Expression of MTHFD2 in peripheral blood mononuclear cell (PBMC) ($n = 21$) and CD14 + monocytes ($n = 14$–22) from HDs and RA patients measured by RT-qPCR. **B** BMMs MTHFD2 level of CIA mice compared to that of WT mice ($n = 3$). **C** Correlation between MTHFD2 level of CD14 + monocytes in RA patients with serum CTX-1 and TRAP5b ($n = 22$). **D** MTHFD2 expression in synovium of OA and RA patients detected by IHC and semi-quantitatively analyzed by ImageJ ($n = 3$). Scale bars = 50 μm. **E** MTHFD2 expression in synovium of WT and CIA mice detected by IHC and semi-quantitatively analyzed by ImageJ ($n = 3$). Scale bars = 50 μm. **F**, **G** Protein level (**F**) and mRNA level (**G**) of MTHFD2 during osteoclast formation in human- and mice-derived OCPs ($n = 3$). **H** Murine MTHFD2 mRNA level at day 5 after RANKL stimulation was assessed for correlation to Ctsk and Atp6v0d2 mRNA level ($n = 11$). Symbols represent individual subjects in independent analysis. Data are shown as mean ± SD. ** = $P < 0.01$; *** = $P < 0.001$, **** = $P < 0.0001$, by Student's t-test (**A**, **B**, **D**, **E**) and one-way ANOVA (**F**, **G**)

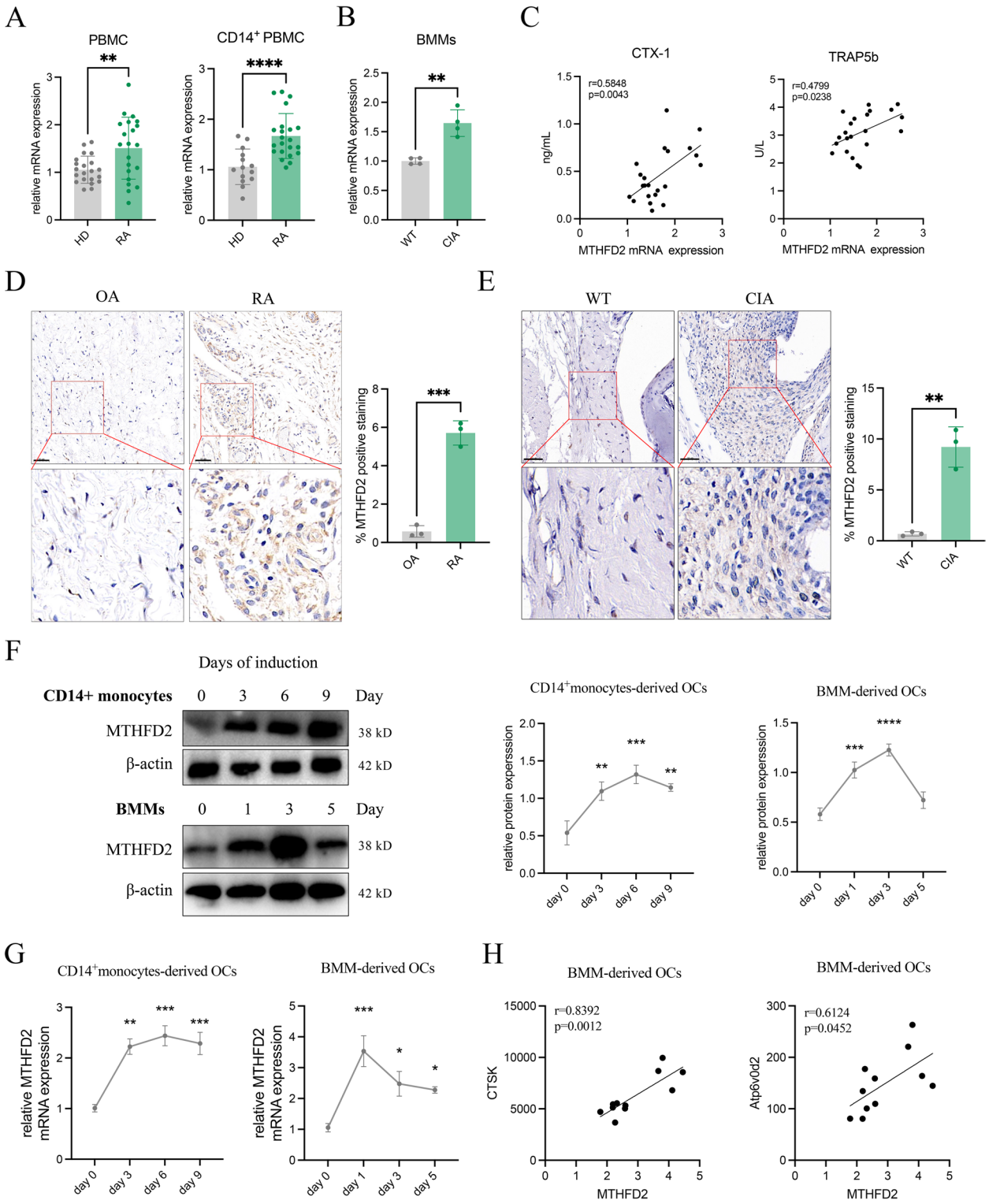

Fig. 1 (See legend on previous page.)

are bone turnover markers (Fig. 1C). IHC was performed on synovium specimens of RA and OA patients. Knee joint tissues were collected from CIA and WT mice. IHC results revealed significantly higher MTHFD2 expression in RA samples compared to OA or WT group, respectively (Fig. 1D, E).

Next, we evaluated the expression of MTHFD2 during osteoclastogenesis. Human and murine OCPs were stimulated with RANKL for osteoclast differentiation, and we observed that the protein and mRNA levels of MTHFD2 were upregulated in both human CD14 + monocytes and murine BMMs after RANKL stimulation (Fig. 1F, G). Further, there was a strong positive correlation between the MTHFD2 mRNA expression and cathepsin K (CTSK) mRNA level ($r = 0.8392$, $p = 0.0012$) and d2 isoform of the vacuolar (H +) ATPase V0 domain (Atp6v0d2) mRNA level ($r = 0.6124$, $p = 0.0452$) in BMMs after RANKL stimulation (Fig. 1H). These results suggest that MTHFD2 expression is upregulated in inflammatory arthritis and is substantially induced during osteoclast formation.

Inhibition of MTHFD2 attenuates osteoclastogenesis

To determine whether MTHFD2 is involved in the osteoclast differentiation, we firstly inhibited MTHFD2 using a highly potent and selective inhibitor (MTHFD2i; DS18561882) and found that pharmacological inhibition of MTHFD2 (7.5 μM) disrupted the differentiation of human OCPs into multinucleated TRAP-positive cells without affecting cell viability (Fig. 2A, Additional file 1: Fig. S2A). Given the importance of actin cytoskeleton organization for osteoclast activation, spreading and function, we stained actin filaments using Alexa Fluor-488 conjugated phalloidin and found that MTHFD2i-treated OCPs had decreased actin belt formation, which may impair their function (Fig. 2B). Accordingly, MTHFD2i substantially suppressed RANKL-induced osteoclast-related gene expression, including tumor necrosis factor receptor superfamily, member 11A gene (*Tnfrsf11a*), nuclear factor of activated T-cells 1 (*Nfatc1*), *Ctsk*, TRAP-encoded gene *Acp5*, matrix metalloproteinase 9 (*Mmp9*), *Atp6v0d2*, and β3 integrin gene *Itgb3* (Fig. 2C). Subsequently, we isolated primary BMMs from mice, followed by RANKL stimulation in the presence or absence of 10 μM MTHFD2i. We found that MTHFID2i treatment did not cause toxic effects in BMMs as well, and that the trends in TRAP positive osteoclast formation and F-actin organization in the MTHFD2i-treated BMMs were similar as that of human OCPs (Fig. 2D, E, Additional file 1: Fig. S2B). Accordingly, RT-qPCR and Western blot analysis showed a marked reduction in the expression of osteoclast-associated markers after MTHFD2i treatment (Fig. 2F, G). Bone resorption activity was also reduced by pharmacological MTHFD2 inhibition, as evidenced by fewer resorption pits on cortical bovine bone slices (Fig. 2H). The differentiation of OCPs into osteoclasts is a multistep process. To clarify the stage at which MTHFD2i suppressed osteoclast formation, we did a time-course experiment of RANKL-induced osteoclast differentiation and added MTHFD2i at the early stage (1–2 days) or later stage (3–4 days) of differentiation. We noted a significant reduction in the number of TRAP-positive cells during the early stage rather than the later stage of differentiation after MTHFD2i treatment (Additional file 1: Fig. S2C). Collectively, these data suggest that pharmacological MTHFD2 inhibition suppressed RANKL-induced osteoclast differentiation and function at the initiation stage.

MTHFD2 is a positive regulator of osteoclast differentiation

To further elucidate the role of MTHFD2 in osteoclastogenesis, an adenoviral vector with specific targeting MTHFD2 shRNA was used to knock down MTHFD2 gene and protein expression in murine BMMs. Both mRNA and protein levels of MTHFD2 in the knockdown group were significantly lower than that in the negative control (NC) group (Additional file 1: Fig. S3A). In accordance with MTHFD2i treatment, MTHFD2 silencing in murine BMMs inhibited RANKL-induced osteoclast formation and decreased osteoclast number and spreading area (Fig. 3A, B); MTHFD2 knockdown also reduced the levels of a series of osteoclast markers (Fig. 3C). Western blot analysis confirmed decreased cytoplasmic levels of CTSK, c-Src, MMP-9, and IGTB3 in MTHFD2-knockdown osteoclasts (Fig. 3D). Overexpression (OE) of MTHFD2 using a lentiviral system in murine BMMs significantly enhanced osteoclast differentiation as evidenced by a significant increase in TRAP-positive osteoclasts and the formation of the F-actin belts (Fig. 3E, F, Additional file 1: Fig. S3B). In conformity, MTHFD2 OE positively regulated the mRNA and protein levels of osteoclast-specific markers (Fig. 3G, H). Together, these data suggest that MTHFD2 plays a critical role in osteoclastogenesis.

MTHFD2 promotes osteoclast differentiation by increasing OXPHOS and ATP production

To better understand the potential mechanisms by which MTHFD2 promotes osteoclastogenesis, RNA-sequencing was performed in RANKL-induced OCPs in the presence or absence of MTHFD2i for 48 h (Additional file 1: Fig. S4A, B). Using a minimum of two-fold change and an adjusted p-value of < 0.05 as cutoff, MTHFD2 inhibition significantly altered the expression of 907 unique transcripts with 228 upregulated genes and 679 downregulated genes (Fig. 4A). GO analysis revealed that "osteoclast differentiation," "bone resorption," and "positive regulation of bone resorption" were among the ten most significantly enrichments with the downregulated genes, corroborating our in vitro results (Additional file 1: Fig. S4C). KEGG pathway analysis showed a strong enrichment of oxidative phosphorylation (OXPHOS) pathway with the genes downregulated

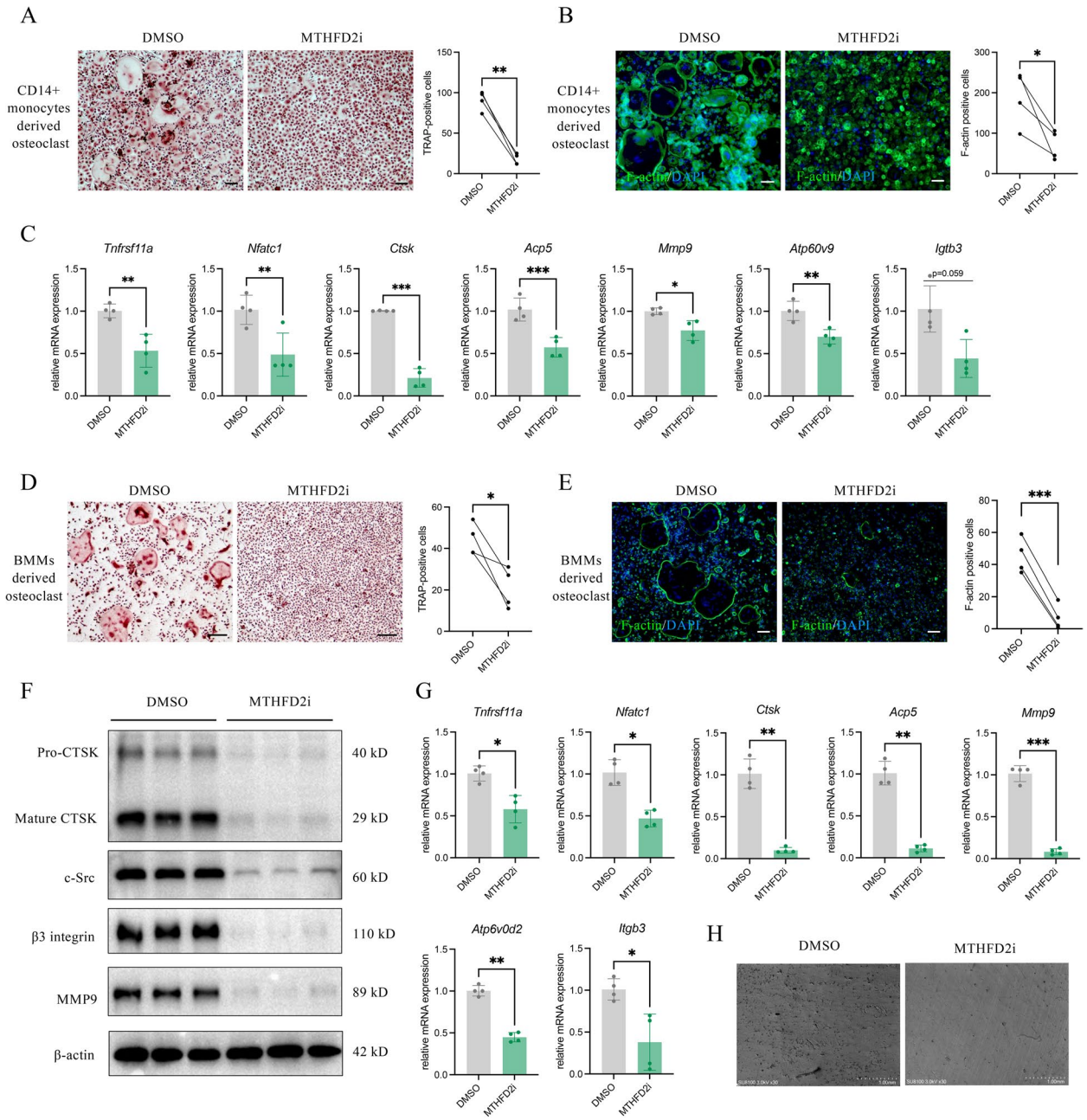

Fig. 2 Suppression of osteoclastogenesis through MTHFD2 inhibition. **A**, **B** Representative images of TRAP (**A**) and F-actin staining (**B**) of CD14 + monocyte-derived osteoclasts treated with DMSO or MTHFD2i ($n = 4$). Scale bars = 100 μm. **C** Expression of Tnfrsf11a, Nfatc1, Ctsk, Acp5, Mmp9, Atp6v0d2, and Itgb3 following 7.5 μM MTHFD2i treatment in CD14 + OCPs ($n = 4$). **D**, **E** Representative images of TRAP (**D**) and F-actin staining (**E**) of BMM-derived osteoclasts treated with DMSO or MTHFD2i ($n = 4$). Scale bars = 100 μm. **F**, **G** Protein level ($n = 3$) (**F**) and mRNA level ($n = 4$) (**G**) of osteoclast-associated markers following 10 μM MTHFD2i treatment in murine OCPs. **H** Bone resorption pits of BMMs-derived osteoclasts were detected by scanning electron microscopy. Scale bars = 1 mm. Data are shown as mean ± SD. * = $P < 0.05$; ** = $P < 0.01$; *** = $P < 0.001$, by Student's t test

after MTHFD2i treatment, which was confirmed by GSEA (Fig. 4B, C). Further, we found that MTHFD2i markedly reduced the levels of representative mitochondrial DNA-encoded respiratory chain subunits (CI, CII, CIII, and CV), which are crucial for OXPHOS (Fig. 4D). We then performed extracellular flux assay and analyzed OCR. Most parameters of OCR, including basal respiration, ATP-coupled respiration, proton

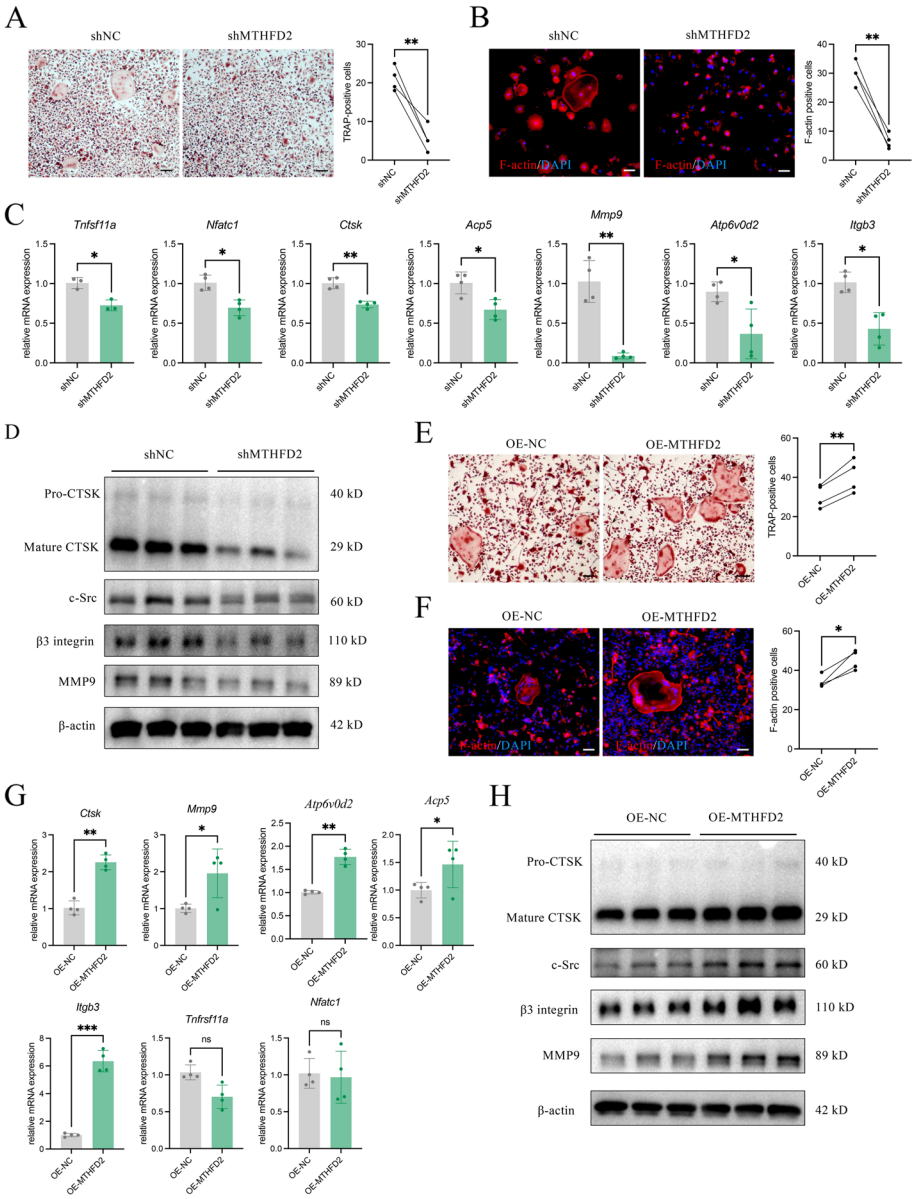

Fig. 3 MTHFD2 level regulates the differentiation of osteoclasts. **A** Representative images of TRAP staining of BMMs from WT mice transfected with short hairpin RNA for MTHFD2 knockdown (sh-MTHFD2) compared to NC group ($n = 4$). Scale bars = 100 μm. **B** Representative images of F-actin staining of sh-MTHFD2 BMMs compared to NC group ($n = 4$). Scale bars = 50 μm. **C**, **D** Expression of osteoclast markers in murine osteoclasts with MTHFD2 knockdown and RANKL stimulation ($n = 3$–4). **E** Representative images of TRAP staining of BMMs transfected with lentivirus containing murine full-length MTHFD2 cDNA vector (OE-MTHFD2) ($n = 4$). Scale bars = 100 μm. **F** Representative images of F-actin staining of OE-MTHFD2 BMMs ($n = 4$). Scale bars = 50 μm. **G**, **H** Expression of osteoclast markers in murine osteoclasts with MTHFD2 overexpression and RANKL stimulation ($n = 3$–4). Data are shown as mean ± SD. * = $P < 0.05$; ** = $P < 0.01$; *** = $P < 0.001$, by Student's t test

leak, and maximal respiration were downregulated in MTHFD2i-treated cells (Fig. 4E, F). Moreover, ATP levels were likewise significantly decreased in MTHFD2i-treated OCPs (Fig. 4G). Meanwhile, MTHFD2-OE could promote the process of cellular OXPHOS as evidenced by increases in basal respiration, maximal respiration, non-mitochondrial respiration, and ATP concentration. (Additional file 1: Fig. S5A, B). Of note, when assessing the number and morphology of mitochondria in OCPs by Mitotracker Green staining and TEM, no significant differences were observed (Fig. 4H, Additional file 1: Fig. S5C, D). Consistent with these findings, mitochondrial markers including translocase of outer mitochondrial membrane 20 (TOMM20) and voltage-dependent

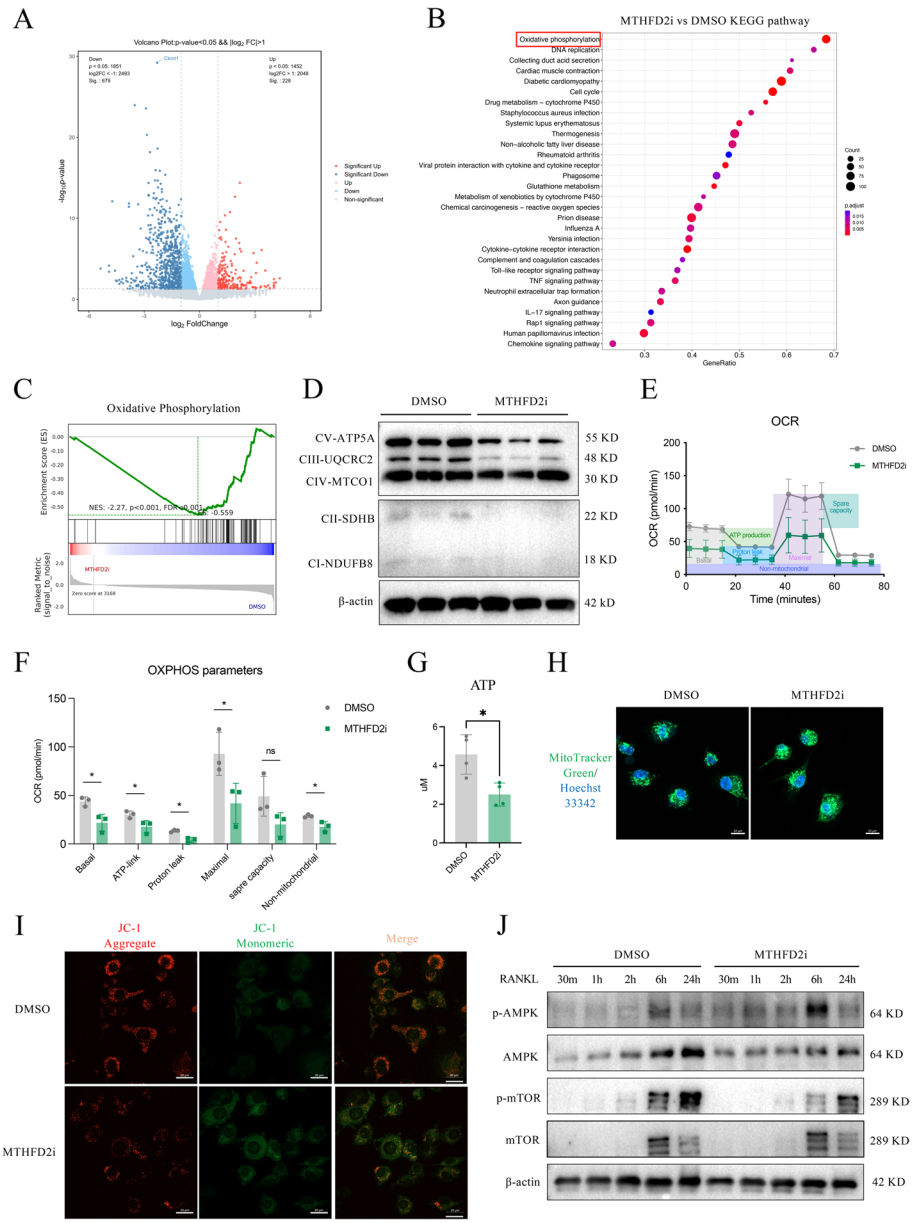

Fig. 4 MTHFD2 controls OXPHOS and ATP production in RANKL-stimulated BMMs. **A** Volcano plot showing differentially expressed genes and decreased Ckmt1 mRNA in MTHFD2i-treated OCPs versus DMSO-treated OCPs ($n=4$). **B** Downregulated KEGG pathway enrichment results from RNA sequencing data in murine OCPs supplemented or not with 10 μM MTHFD2i for 48 h ($n=4$). **C** GSEA results indicating significant difference in OXPHOS comparing MTHFD2i versus DMSO group ($n=4$). Pathways with an adjusted p-value less than 0.05 are considered significantly enriched. **D** Representative ETC markers in OCPs were detected by Western blot ($n=3$). **E**, **F** OCR (**E**) and mitochondrial function parameters (**F**) were analyzed by extracellular flux assay in OCPs stimulated with RANKL for 72 h (n = 3). **G** ATP levels of OCPs treated with DMSO or MTHFD2i ($n=4$). **H** Representative images of Mitotracker Green staining in OCPs at day 3 ($n=3$). Scale bars = 10 μm. **I** Representative images of JC-1 staining in OCPs at day 3 ($n=3$). Scale bars = 20 μm. **J** Phosphorylation of AMPK and mTOR after MTHFD2i treatment at indicated time ($n=3$). Data are shown as mean ± SD. ns = not significant, * = $P<0.05$; ** = $P<0.01$; *** = $P<0.001$, by Student's t test

anion channel (VDAC) remained unaltered (Additional file 1: Fig. S5E). Peroxisome proliferator-activated receptor gamma coactivators-1β (PGC1β), which promotes mitochondrial biogenesis, was decreased after MTHFD2i treatment. However, lentiviral-mediated PGC1β reintroduction failed to rescue osteoclast differentiation and function (Additional file 1: Fig. S5F). We also tested the effect of MTHFD2i on the expression of key molecules that are involved in autophagy and mitophagy by qRT-PCR and we found that there are no differences in

the tested genes, indicating that the suppressive capacity of OXPHOS and ATP production was independent of autophagy or mitophagy (Additional file 1: Fig. S6).

Next, we analyzed the mitochondrial membrane potential in OCPs using dual-emission potentiometric dye JC-1. Upon stimulation with RANKL, a high proportion of red-labeled versus green-labeled fluorescence intensity indicated an active mitochondrial electron transport chain (ETC) function. However, the ratio of red/green fluorescence intensity was noticeably reduced in MTHFD2i treatment group, indicating an impaired mitochondrial membrane potential (Fig. 4I). As mitochondrial respiratory chain is a major source of reactive oxygen species (ROS) generation, we further examined mitochondrial ROS levels by MitoSOX Red staining. Due to low ETC function, decreased mitochondrial ROS generation was observed following MTHFD2 inhibition (Additional file 1: Fig. S7A, B). Impaired ETC activity also resulted in reduced NAD + regeneration and a decreased ratio of NAD + /NADH (Additional file 1: Fig. S7C). To determine whether increasing NAD + concentration could rescue MTHFD2i-treated osteoclast formation, we added β-nicotinamide mononucleotide (NMN) to culture media, a product of the nicotinamide phosphoribosyltransferase reaction and a key NAD^+ intermediate. However, the addition of NMN did not improve osteoclast generation in the presence of MTHFD2i (Additional file 1: Fig. S7D).

AMP-activated protein kinase (AMPK) plays a key role in restoring metabolic homeostasis [30]. Once cellular ATP is depleted, AMPK is activated and further inhibits the phosphorylation of mammalian target of rapamycin (mTOR), a downstream target of AMPK, leading to the initiation of catabolic pathways to augment ATP production while turning off synthetic pathways that consume ATP [31, 32]. Here, we observed that after RANKL stimulation, AMPK was rapidly activated accompanied with a significant low level of mTOR phosphorylation in MTHFD2i-treated OCPs, demonstrating a low energy status and increased energy stress (Fig. 4J). Together, our findings suggest that MTHFD2 can effectively increase RANKL-induced OXPHOS and ATP production to support osteoclastogenesis.

MTHFD2 regulates CKMT1 expression during osteoclast differentiation

To identify potential MTHFD2 targets that promote OXPHOS and thus osteoclast formation, we investigated the differentially expressed gene profiles of MTHFD2i- versus DMSO-treated OCPs. Mitochondrial creatine kinase 1 (CKMT1) was one of the most strongly downregulated genes upon MTHFD2 inhibition (Fig. 4A). CKMT1 is an isoform of creatine kinase (CK) family and is implicated in ATP production and osteoclastogenesis [33, 34]. We validated that MTHFD2i-treated osteoclasts displayed markedly decreased mRNA and protein levels of CKMT1 (Fig. 5A, B). Similarly, CKMT1 protein expression was also downregulated in shMTHFD2 OCPs compared to the NC group (Fig. 5C). Nonetheless, no increasing CKMT1 level was observed in OE-MTHFD2 OCPs (Additional file 1: Fig. S8). As expected, creatine kinase activity was significantly reduced in MTHFD2i-treated OCPs (Fig. 5D). Phosphocreatine (Pcr), a product of CK-mediated enzymatic reaction, has been shown to activate the creatine pathway, thereby rescuing decreased intracellular ATP level and restoring normal mitochondrial respiration capacity [35]. We conducted complementary rescue experiments to investigate the functional importance of CKMT1 in osteoclast differentiation. The addition of exogenous Pcr significantly enhanced RANKL-induced osteoclast formation and actin ring formation in the presence of MTHFD2i (Fig. 5E, F). Moreover, expression of osteoclast-associated markers was rescued by Pcr in the MTHFD2i-treated cells (Fig. 5G). Western blot showed that exogenous Pcr partly rescued the level of ETC components CIII and CV as well (Fig. 5H). These results underscore a key role of CKs in participating in MTHFD2 mediated osteoclastogenesis.

MTHFD2 knockdown ameliorates pathological bone resorption in CIA mice

To investigate the potential of targeting MTHFD2 in protecting against inflammatory bone loss, we analyzed bone mass in CIA mice with local aav injection for MTHFD2 knockdown in the knee joints (Fig. 6A). The effectiveness of MTHFD2 silencing was confirmed by Western blot (Additional file 1: Fig. S9A). Local MTHFD2 knockdown did not lead to significant reduction of clinical arthritis scores (Fig. 6B, Additional file 1: Fig. S9B), nor observed difference in murine weight (Additional file 1: Fig. S9C). However, μCT reconstruction of the tibial revealed that MTHFD2 knockdown ameliorated bone destruction with significant increases in bone volume and Tb.N, Tb.Th, and BMD (Fig. 6C, D, Additional file 1: Fig. S9D). Moreover, TRAP staining demonstrated a marked enhancement of osteoclast quantity in CIA mice of NC group, whereas MTHFD2 knockdown reduced tibial osteoclast number and size (Fig. 6E, F). Additionally, reduced expression of several osteoclast markers, including CTSK, MMP9, and ITGB3, were found in knee joint cells from MTHFD2-knockdown mice (Additional file 1: Fig. S9E). To test whether the high bone mass phenotype observed in aav-MTHFD2 mice resulted from reduced osteoclast activity without changes in the osteoblast compartment, we performed toluidine blue staining and OCN staining to analyze the osteoblast number and function in tibial bone

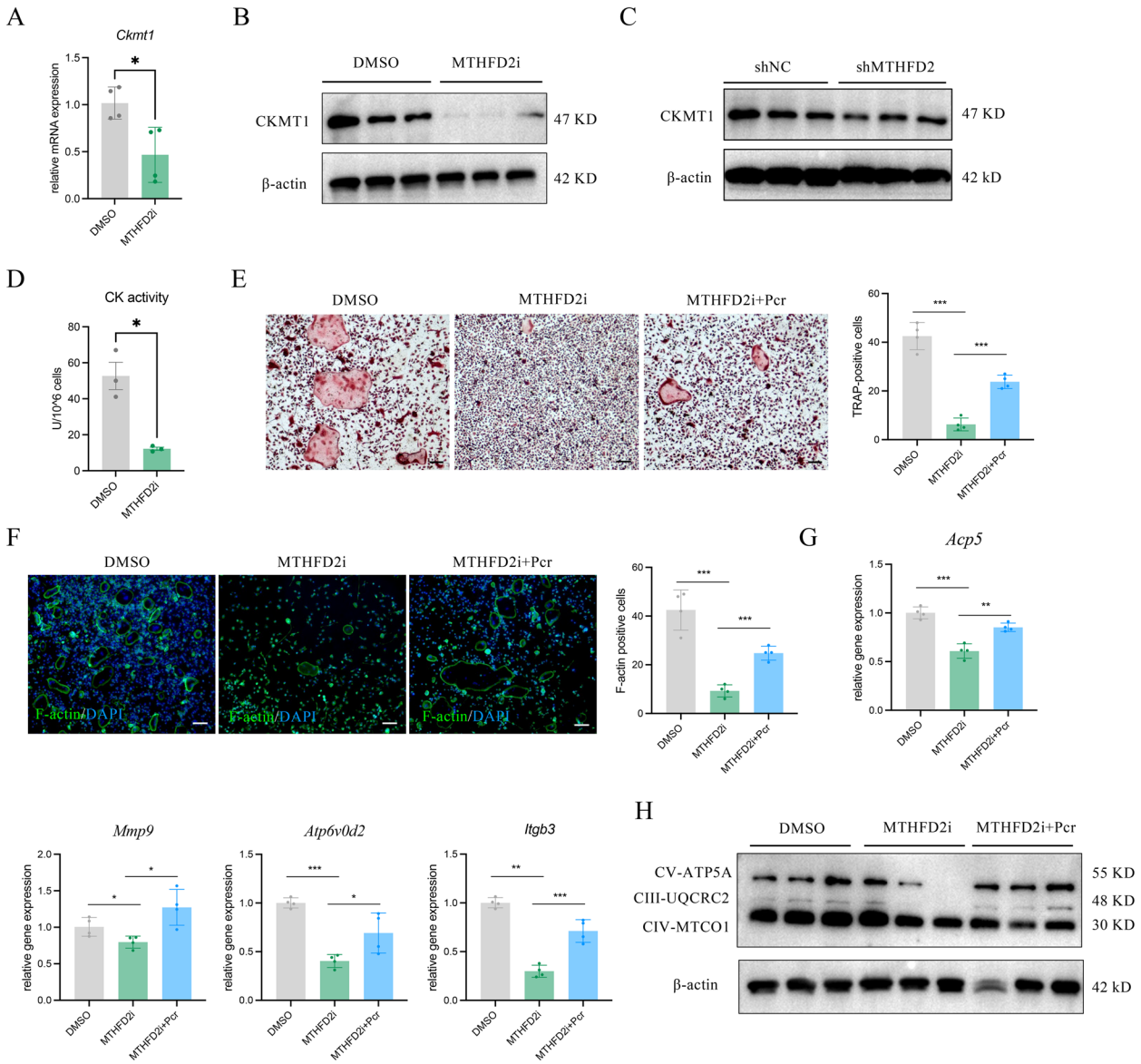

Fig. 5 MTHFD2 regulates osteoclastic creatine kinases expression. **A**, **B** Relative mRNA (**A**) and protein (**B**) expression of CKMT1 following MTHFD2i treatment for 72 h ($n = 3$). **C** Relative protein expression of CKMT1 in MTHFD2-knockdown OCPs ($n = 3$). **D** Cellular creatine kinase activity of MTHFD2i-treated OCPs compared to control group ($n = 4$).**E**, **F** Representative images of TRAP staining (**E**) and F-actin staining (**F**) of OCPs stimulated with DMSO, MTHFD2i, or MTHFD2i+Pcr ($n = 4$). Scale bars = 100 μm. **G** Expression of osteoclast markers in murine osteoclasts with MTHFD2i, Pcr and RANKL stimulation ($n = 4$). **H** Representative ETC markers in MTHFD2i-treated OCPs following Pcr rescue were detected by Western blot (n=3). Data are shown as mean ± SD. * = $P < 0.05$; ** = $P < 0.01$; *** = $P < 0.001$, by Student's t test

sections. As shown in Fig. 6G and H, osteoblasts number remained unchanged between two groups. Together, these findings suggest that MTHFD2 knockdown ameliorates inflammatory bone loss by reducing osteoclast numbers without affecting osteoblast function.

Discussion

Osteoclasts are the only cells capable of bone degradation in physiologic and pathologic contexts [36]. Recent findings have highlighted that differentiation of osteoclasts is accompanied by dynamic metabolic reprogramming; however, the role of cellular metabolic changes in shaping osteoclast formation remains to be elucidated. In this study, we demonstrated that MTHFD2 is upregulated in RA and during osteoclastogenesis. MTHFD2 positively regulates osteoclast formation and MTHFD2 silencing leads to an increased bone mineral density. Blockade of MTHFD2 function primarily dampens osteoclast differentiation by suppressing OXPHOS and energy metabolism through targeting CKMT1 at the early phase.

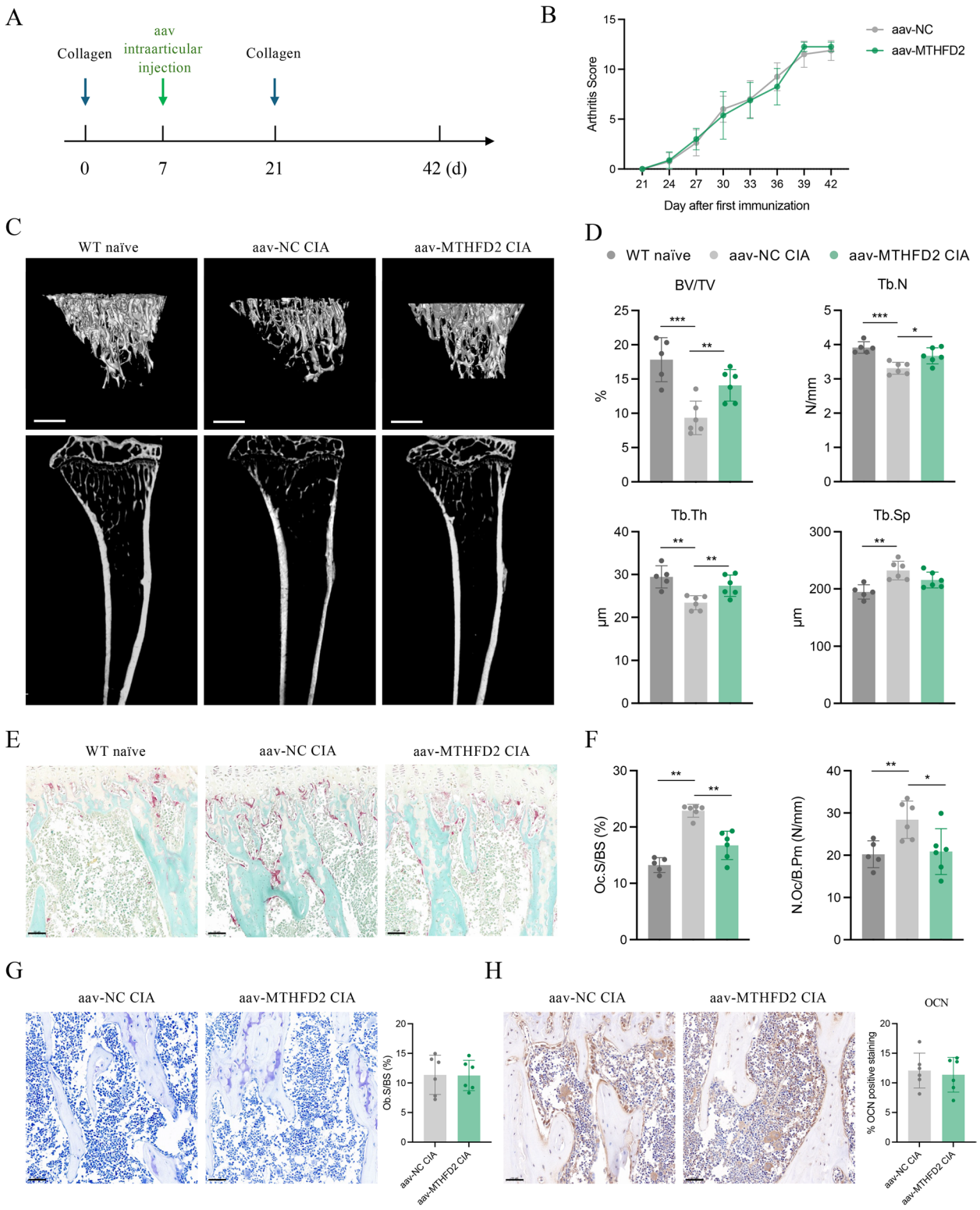

Fig. 6 MTHFD2 knockdown suppresses pathological bone resorption in vivo. **A** Schematic of CIA induction and intraarticular aav injection. **B** Arthritis scores were evaluated every three days ($n = 6$). **C, D** Representative tibial μCT images (**C**) and quantification of BV/TV, Tb.N, Tb.Th, and Tb.Sp (**D**) in WT-naïve, aav-NC CIA, and aav-MTHFD2 CIA groups ($n = 5$–6). **E, F** Representative images of TRAP staining (**E**) and quantification of Oc.N/BS and Oc.S/B.Pm of the tibia (**F**) ($n = 5$–6). Scale bars=50 μm. **G** Representative toluidine blue staining images of the tibia and quantification of Ob.S/BS ($n = 6$). Scale bars = 50 μm. **H** Representative OCN IHC sections of the tibia and quantitative analysis ($n = 6$). Scale bars = 50 μm. Data are shown as mean ± SD. * = $P < 0.05$; ** = $P < 0.01$; *** = $P < 0.001$, by Student's *t* test

Collectively, we show a hitherto undiscovered role of MTHFD2 on bone homeostasis which primarily exerts its regulatory effects on osteoclastogenesis through OXPHOS and energy metabolism, offering potential therapeutic applications for diseases associated with exaggerated bone resorption.

The immunomodulatory capacities of MTHFD2 have gained increasing attention in recent years. Sugiura et al. identified MTHFD2 as a metabolic checkpoint that regulates de novo purine synthesis and directs T cell proliferation, differentiation, and cytokine production [37]. MTHFD2i treatment has been shown to ameliorate multiple inflammatory diseases in vivo, including models of Delayed Type Hypersensitivity, Experimental Autoimmune Encephalomyelitis, and inflammatory bowel disease [37]. Moreover, MTHFD2 depletion could impair germinal center B cell frequency and responses such as antigen-specific antibody production [38]. It also played key roles in Epstein-Barr virus-driven B cell growth and survival, which causes B cell lymphomas [39]. Notably, several reports highlighted the crucial roles of MTHFD2 in protecting mitochondrial function. Previous work has demonstrated that in embryonic stem cells, mitochondrial MTHFD2 preserves the integrity of the mitochondrial respiratory chain and prevents mitochondrial dysfunction by interacting with ETC Complex III [40]. Moreover, MTHFD2 activates mitochondrial metabolism and promotes prostate cancer cell proliferation, whereas MTHFD2i with enzalutamide inhibits castration-resistant prostate cancer progression [41]. Likewise, MTHFD2 promotes basal and maximal extracellular acidification rate in renal cell carcinoma cells [42]. In our study, MTHFD2 is a potent regulator in orchestrating mitochondrial respiratory activity critical for the differentiation of both murine and human OCPs. During osteoclastogenesis, MTHFD2i predominantly inhibits OXPHOS and ATP production, which disrupts the mitochondrial membrane potential and results in AMPK-mTOR activation and reduced mitochondrial superoxide levels. In CIA mice, MTHFD2 silencing ameliorates bone loss by reducing the number of osteoclasts without affecting osteoblasts. The reason aav-mediated knockdown primarily impacts osteoclasts may be attributed to the extremely low expression of MTHFD2 in osteoblasts (data not shown), which renders the effect of MTHFD2 knockdown on osteoblasts negligible.

Upregulation of energy metabolism is a hallmark of osteoclastogenesis; RANK/RANKL signaling promotes mitochondrial respiration and ATP production to meet the intensely increased energy requirements [43]. Mitochondria generate energy mainly through OXPHOS, the most efficient way to supply energy, which has been identified as the primary bioenergetic source of ATP for osteoclastogenesis [14]. In contrast, glycolysis serves as the major metabolic pathway that meets ATP demand during mature osteoclasts-mediated bone resorption [14]. Efficient energy metabolism is essential for the proper functioning of each stage. The reprogramming of energy metabolism in immune cells governs cell fate and function. OXPHOS generates ATP through reactions occurring in ETC, which includes complexes I, II, III, IV, and ATP synthase enzyme (Complex V). Deletion of ETC Complex I subunit Ndufs4 has been reported to cause mitochondrial dysfunction and failure of osteoclastogenesis, underscoring the critical role of mitochondrial function and ATP generation for osteoclast differentiation [44]. Interestingly, our RNA-seq data revealed that MTHFD2 inhibition predominantly attenuates OXPHOS during osteoclast differentiation, unveiling the potential of MTHFD2i to suppress the generation and function of osteoclasts by interfering with intrinsic energy metabolic pathways. Since osteoclasts are in a state of high-energy demand, mitochondrial biogenesis is also promoted during differentiation [45]. PGC1β acts as a master regulator of mitochondrial biogenesis and respiration of osteoclasts, which has been linked to osteoclast activation and bone destruction in RA and osteoporosis [45, 46]. Interestingly, recent studies have shown that mitochondrial biogenesis and genetic deletion of PGC1β impair bone resorbing function of osteoclasts but not their differentiation [47]. In conformity, our data demonstrated that, although PGC1β was decreased following MTHFD2 inhibition, PGC1β reintroduction was unable to rescue osteoclast formation.

CKs play vital roles in preserving cellular energy balance by facilitating the reversible transfer of phosphate groups between ATP and creatine, leading to the production of phosphocreatine and ADP [48]. Recent studies have underscored the significant role of CKs in regulating OXPHOS. Brain-type cytoplasmic creatine kinase silencing was shown to significantly attenuate OXPHOS and ATP generation without affecting mitochondrial mass [49]. Likewise, depletion of CKMT1 directly disrupts mitochondrial homeostasis and impairs OXPHOS in intestinal epithelial cells and cancer cells, thus being a promising therapeutic target [35, 50, 51]. During osteoclastogenesis, RANKL stimulation upregulates CKMT1 expression to generate substantial amount of phosphocreatine, which acts as a cellular energy reservoir and provides ATP at sites where high energy is required [52]. In this study, we demonstrated that CKMT1 expression and cellular CK enzymatic activity were reduced during osteoclastogenesis when suppressing MTHFD2 activity using inhibitor and shRNA knockdown system. Despite the addition of phosphocreatine could promote osteoclast formation, several questions remain unanswered.

One limitation of this work is that the mechanistic regulation of CKMT1 by MTHFD2 inhibition has yet to be investigated. In addition, more validation of the link between CKMT1 and OXPHOS following MTHFD2 inhibition would be beneficial.

Conclusions

In summary, we showed that RANKL increases MTHFD2 expression, and we identified that MTHFD2 inhibition significantly suppressed CKMT1 expression, which, in turn, affected OXPHOS and ATP production, eventually impaired osteoclastogenesis and inflammatory bone resorption in vitro and in vivo. Hence, targeting MTHFD2 may serve as a promising therapeutic approach to improve inflammatory bone loss.

Abbreviations

RA	Rheumatoid arthritis
MTHFD2	Methylenetetrahydrofolate dehydrogenase 2
BMMs	Bone marrow macrophages
CIA	Collagen-induced arthritis
OXPHOS	Oxidative phosphorylation
ATP	Adenosine triphosphate
CKMT1	Mitochondrial creatine kinase 1
bDMARDs	Biologic disease-modifying antirheumatic drugs
RANKL	Receptor activator of nuclear factor-κB ligand
BMD	Bone mineral density
1C	One-carbon
MTX	Methotrexate
DHFR	Dihydrofolate reductase
HDs	Healthy donors
OA	Osteoarthritis
ACR	American College of Rheumatology
EULAR	European League Against Rheumatism
PBMCs	Peripheral blood mononuclear cells
ELISA	Enzyme-linked immunosorbent assay
CTX-1	C-terminal telopeptides of type I collagen
TRAP	Tartrate-resistant acid phosphatase
WT	Wildtype
α-MEM	α Minimum essential medium
OCPs	Osteoclast precursors
qRT-PCR	Quantitative real-time polymerase chain reaction
shRNA	Short hairpin RNA
DEGs	Differentially expressed genes
GO	Gene Ontology
KEGG	Kyoto Encyclopedia of Genes and Genomes
GSEA	Gene Set Enrichment Analysis
OCR	Oxygen consumption rate
TEM	Transmission electron microscopy
aav	Adeno-associated virus
BV/TV	Bone volume/total volume
Tb.N	Trabecular bone number
Tb.Th	Trabecular bone thickness
Tb.Sp	Trabecular bone separation
OCN	Osteocalcin
IHC	Immunohistochemistry
Oc.S/BS	Osteoclast surface/bone surface
N.Oc./B.Pm.	Osteoclast number/bone perimeter
Ob. S/BS	Osteoblast surface/bone surface
ANOVA	Analysis of variance
CTSK	Cathepsin K
Atp6v0d2	D2 isoform of the vacuolar (H+) ATPase V0 domain
Tnfrsf11a	Tumor necrosis factor receptor superfamily, member 11A
Nfatc1	Nuclear factor of activated T-cells 1
Mmp9	Matrix metalloproteinase 9
Itgb3	β3 Integrin
NC	Negative control
OE	Overexpression
TOMM20	Translocase of outer mitochondrial membrane 20
VDAC	Voltage-dependent anion channel
PGC1β	Peroxisome proliferator-activated receptor gamma coactivators-1β
ETC	Electron transport chain
ROS	Reactive oxygen species
NMN	β-Nicotinamide mononucleotide
AMPK	AMP-activated protein kinase
mTOR	Mammalian target of rapamycin
CK	Creatine kinase
Pcr	Phosphocreatine

Supplementary Information

The online version contains supplementary material available at https://doi.org/10.1186/s12916-025-03945-y.

Additional file 1. Figs. S1-S9. Fig S1- [Purification rate of CD14+ PBMCs]. Fig S2- [Cytotoxicity and effects of MTHFD2i on different stages of osteoclastogenesis]. Fig S3- [Expression of MTHFD2 in adenovirus or lentivirus transfected BMMs]. Fig S4- [Gene expression profile of RNA-sequencing and Gene Ontologyanalysis]. Fig S5- [Mitochondrial respiration, mitochondria morphology and mitochondrial markers expression after MTHFD2 OE or MTHFD2i treatment]. Fig S6- [mRNA level of autophagy and mitophagy markers in OCPs]. Fig S7- [MitoSOX staining and NAD/NADH ratio of OCPs treated with DMSO or MTHFD2i]. Fig S8- [Expression of CKMT1 after MTHFD2 OE]. Fig S9- [CIA model establishment and osteoclast-specific markers in MTHFD2 knockdown CIA mice].

Additional file 2. Original images of all western blots analyzed in the present study.

Acknowledgements

We thank Prof. Ren Xu (Xiamen University) for providing Osteomeasure software and assistance with bone histomorphometry. We thank all study participants and the research staff who participated in this work.

Authors' contributions

Z.C. and C.Y. directed the study design and revised the manuscript. Y.L. and M.C. performed the cell and molecular experiments and animal experiments and drafted the initial manuscript. Y.Q., X.D., L.L. and X.W. conducted part of the animal experiments. Y.L., Z.L. and H.J. conducted the statistical analyses. All authors read and approved the final manuscript.

Funding

This work was supported by the National Natural Science Foundation of China (Grant No. 82471819 and 81871227, to ZC), Anhui Provincial Natural Science Foundation (Grant No. 2408085J046 to ZC), Anhui Provincial Key Research and Development Plan (No. 2022h11020009 to ZC), and the Fundamental Research Funds for the Central Universities (No. YD9110002012 to ZC).

Data availability

All the data generated in this study were shown in the main text and supplementary material. Additional information is also available upon reasonable request to the corresponding authors.

Declarations

Ethics approval and consent to participate

All experiments were approved by the Medical Ethics Committee of the First Affiliated Hospital of University of Science and Technology of China (2023KY-438). Experiments were conducted in accordance with relevant institutional guidelines and regulations.

Consent for publication

Not applicable.

Competing interests
The authors declare no competing interests.

Author details
[1]Department of Rheumatology and Immunology, the First Affiliated Hospital of USTC, Division of Life Sciences and Medicine, University of Science and Technology of China, Hefei 230001, China. [2]Department of Internal Medicine 3, Rheumatology and Immunology, Friedrich Alexander University Erlangen-Nuremberg and Universitätsklinikum Erlangen, Erlangen, Germany. [3]The MED-X Institute, Center for Cancer Precision Medicine, First Affiliated Hospital of Xi'an Jiaotong University, Xi'an Jiaotong University, Building 21, Western China Science and Technology Innovation Harbor, Xi'an 710000, China. [4]Department of Rheumatology and Immunology and The MED-X institute, Center for Immunological and Metabolic Diseases, The First Affiliated Hospital of Xi'an Jiaotong University, Xi'an Jiaotong University, Building 21, Western China Science and Technology Innovation Harbor, Xi'an 710000, China.

Received: 8 October 2024 Accepted: 12 February 2025
Published online: 27 February 2025

References

1. Smith MH, Berman JR. What Is Rheumatoid Arthritis? JAMA. 2022;12:1194.
2. Schett G, Gravallese E. Bone erosion in rheumatoid arthritis: mechanisms, diagnosis and treatment. Nat Rev Rheumatol. 2012;11:656–64.
3. Gough AK, et al. Generalised bone loss in patients with early rheumatoid arthritis. Lancet. 1994;8914:23–7.
4. Welsing PM, et al. The relationship between disease activity, joint destruction, and functional capacity over the course of rheumatoid arthritis. Arthritis Rheum. 2001;9:2009–17.
5. Svensson B, et al. Erosion-free rheumatoid arthritis: clinical and conceptional implications-a BARFOT study. BMC Rheumatol. 2022;1:88.
6. Goltzman D. Discoveries, drugs and skeletal disorders. Nat Rev Drug Discov. 2002;10:784–96.
7. Zerbini CAF, et al. Biologic therapies and bone loss in rheumatoid arthritis. Osteoporos Int. 2017;2:429–46.
8. Takeuchi T, et al. Effects of the anti-RANKL antibody denosumab on joint structural damage in patients with rheumatoid arthritis treated with conventional synthetic disease-modifying antirheumatic drugs (DESIRABLE study): a randomised, double-blind, placebo-controlled phase 3 trial. Ann Rheum Dis. 2019;7:899–907.
9. Dore RK, et al. Effects of denosumab on bone mineral density and bone turnover in patients with rheumatoid arthritis receiving concurrent glucocorticoids or bisphosphonates. Ann Rheum Dis. 2010;5:872–5.
10. Yue J, et al. Repair of Bone Erosion in Rheumatoid Arthritis by Denosumab: A High-Resolution Peripheral Quantitative Computed Tomography Study. Arthritis Care Res (Hoboken). 2017;8:1156–63.
11. Buch MH. Defining refractory rheumatoid arthritis. Ann Rheum Dis. 2018;7:966–9.
12. Ehrenstein V, et al. Osteonecrosis of the jaw among patients with cancer treated with denosumab or zoledronic acid: Results of a regulator-mandated cohort postauthorization safety study in Denmark, Norway, and Sweden. Cancer. 2021;21:4050–8.
13. Elbers LPB, Raterman HG, Lems WF. Bone Mineral Density Loss and Fracture Risk After Discontinuation of Anti-osteoporotic Drug Treatment: A Narrative Review. Drugs. 2021;14:1645–55.
14. Park-Min KH. Metabolic reprogramming in osteoclasts. Semin Immunopathol. 2019;5:565–72.
15. Cao S, et al. L-arginine metabolism inhibits arthritis and inflammatory bone loss. Ann Rheum Dis. 2024;1:72–87.
16. Ducker GS, Rabinowitz JD. One-Carbon Metabolism in Health and Disease. Cell Metab. 2017;1:27–42.
17. Locasale JW. Serine, glycine and one-carbon units: cancer metabolism in full circle. Nat Rev Cancer. 2013;8:572–83.
18. Yuan Y, Shao W, Li Y. Associations between C677T and A1298C polymorphisms of MTHFR and susceptibility to rheumatoid arthritis: a systematic review and meta-analysis. Rheumatol Int. 2017;4:557–69.
19. Kim YI. 5,10-Methylenetetrahydrofolate reductase polymorphisms and pharmacogenetics: a new role of single nucleotide polymorphisms in the folate metabolic pathway in human health and disease. Nutr Rev. 2005;11:398–407.
20. Zhao Z, et al. Application and pharmacological mechanism of methotrexate in rheumatoid arthritis. Biomed Pharmacother. 2022;150:113074.
21. Bleyer WA. The clinical pharmacology of methotrexate: new applications of an old drug. Cancer. 1978;1:36–51.
22. Banka S, et al. Identification and characterization of an inborn error of metabolism caused by dihydrofolate reductase deficiency. Am J Hum Genet. 2011;2:216–25.
23. Wang W, Zhou H, Liu L. Side effects of methotrexate therapy for rheumatoid arthritis: A systematic review. Eur J Med Chem. 2018;158:502–16.
24. Nilsson R, et al. Metabolic enzyme expression highlights a key role for MTHFD2 and the mitochondrial folate pathway in cancer. Nat Commun. 2014;5:3128.
25. Aletaha D, et al. 2010 Rheumatoid arthritis classification criteria: an American College of Rheumatology/European League Against Rheumatism collaborative initiative. Arthritis Rheum. 2010;9:2569–81.
26. Rohatgi N, et al. BAP1 promotes osteoclast function by metabolic reprogramming. Nat Commun. 2023;1:5923.
27. Brand DD, Latham KA, Rosloniec EF. Collagen-induced arthritis. Nat Protoc. 2007;5:1269–75.
28. Ge G, et al. GLI1 facilitates collagen-induced arthritis in mice by collaborative regulation of DNA methyltransferases. Elife. 2023;12:e92142.
29. Yuan L, et al. Major vault protein (MVP) negatively regulates osteoclastogenesis via calcineurin-NFATc1 pathway inhibition. Theranostics. 2021;15:7247–61.
30. Leclerc I, Rutter GA. AMP-activated protein kinase: a new beta-cell glucose sensor?: Regulation by amino acids and calcium ions. Diabetes. 2004;53:S67–74.
31. Xu J, Ji J, Yan XH. Cross-talk between AMPK and mTOR in regulating energy balance. Crit Rev Food Sci Nutr. 2012;5:373–81.
32. Lin SC, Hardie DG. AMPK: Sensing Glucose as well as Cellular Energy Status. Cell Metab. 2018;2:299–313.
33. Chang EJ, et al. Brain-type creatine kinase has a crucial role in osteoclast-mediated bone resorption. Nat Med. 2008;9:966–72.
34. Murata K, et al. Hypoxia-Sensitive COMMD1 Integrates Signaling and Cellular Metabolism in Human Macrophages and Suppresses Osteoclastogenesis. Immunity. 2017(1):66–79 e5.
35. Fenouille N, et al. The creatine kinase pathway is a metabolic vulnerability in EVI1-positive acute myeloid leukemia. Nat Med. 2017;3:301–13.
36. Charles JF, Aliprantis AO. Osteoclasts: more than "bone eaters." Trends Mol Med. 2014;8:449–59.
37. Sugiura A, et al. MTHFD2 is a metabolic checkpoint controlling effector and regulatory T cell fate and function. Immunity. 2022(1):65–81 e9.
38. Wu J, et al. Metabolic determinants of germinal center B cell formation and responses. Nat Chem Biol. 2024. https://doi.org/10.1038/s41589-024-01690-6. Epub ahead of print
39. Wang LW, et al. Epstein-Barr-Virus-Induced One-Carbon Metabolism Drives B Cell Transformation. Cell Metab. 2019(3):539–555 e11.
40. Yue L, et al. Mthfd2 Modulates Mitochondrial Function and DNA Repair to Maintain the Pluripotency of Mouse Stem Cells. Stem Cell Reports. 2020;2:529–45.
41. Zhao R, et al. PPFIA4 promotes castration-resistant prostate cancer by enhancing mitochondrial metabolism through MTHFD2. J Exp Clin Cancer Res. 2022;1:125.
42. Green NH, et al. MTHFD2 links RNA methylation to metabolic reprogramming in renal cell carcinoma. Oncogene. 2019;34:6211–25.
43. Ono T, et al. RANKL biology: bone metabolism, the immune system, and beyond. Inflamm Regen. 2020;3:259–66.
44. Jin Z, et al. Mitochondrial complex I activity suppresses inflammation and enhances bone resorption by shifting macrophage-osteoclast polarization. Cell Metab. 2014;3:483–98.
45. Ishii KA, et al. Coordination of PGC-1beta and iron uptake in mitochondrial biogenesis and osteoclast activation. Nat Med. 2009;3:259–66.
46. Ma JD, et al. Activation of the Peroxisome Proliferator-Activated Receptor gamma Coactivator 1beta/NFATc1 Pathway in Circulating Osteoclast Precursors Associated With Bone Destruction in Rheumatoid Arthritis. Arthritis Rheumatol. 2019;8:1252–64.
47. Zhang Y, et al. PGC1beta Organizes the Osteoclast Cytoskeleton by Mitochondrial Biogenesis and Activation. J Bone Miner Res. 2018;6:1114–25.

48. Wallimann T, et al. Some new aspects of creatine kinase (CK): compartmentation, structure, function and regulation for cellular and mitochondrial bioenergetics and physiology. BioFactors. 1998;3–4:229–34.
49. He L, et al. CKB Promotes Mitochondrial ATP Production by Suppressing Permeability Transition Pore. Adv Sci (Weinh). 2024;31: e2403093.
50. Wang S, et al. Neutrophil-derived PAD4 induces citrullination of CKMT1 exacerbates mucosal inflammation in inflammatory bowel disease. Cell Mol Immunol. 2024;6:620–33.
51. Kurmi K, et al. Tyrosine Phosphorylation of Mitochondrial Creatine Kinase 1 Enhances a Druggable Tumor Energy Shuttle Pathway. Cell Metab. 2018(6):833–847 e8.
52. Zhu L, et al. A Zeb1/MtCK1 metabolic axis controls osteoclast activation and skeletal remodeling. EMBO J. 2023;7: e111148.

Publisher's Note